R. Sadanandan, M. Stöhr, W. Meier, Flowfield-flame structure interactions in an oscillating swirl flame, Combustion, Explosion and Shock Waves 45 (2009) 518-529.

The original publication is available at www.springerlink.com

http://dx.doi.org/10.1007/s10573-009-0063-z

Flowfield-flame structure interactions in an oscillating swirl flame: An investigation using phase resolved and simultaneous OH-PLIF and stereoscopic PIV measurements

Rajesh Sadanandan, Michael Stöhr, Wolfgang Meier

Institut für Verbrennungstechnik, DLR Stuttgart, Pfaffenwaldring 38-40, 70569-Stuttgart, Germany.

Abstract

A swirling CH_4/air diffusion flame at atmospheric pressure was stabilized in a gas turbine model combustor with good optical access. The investigated flame with a thermal power of 10 kW and an overall equivalence ratio of 0.75 exhibited pronounced thermoacoustic oscillations at a frequency of 295 Hz. The main goal of the presented work was a detailed experimental characterization of the flame behavior in order to better understand the flame stabilization mechanism and the feedback loop of the thermoacoustic instability. OH* chemiluminescence imaging was applied for the determination of the flame shape and as a measure of the heat release rate. Laser Raman scattering was used for the simultaneous detection of the major species concentrations, mixture fraction and temperature. The velocity fields were measured by particle image velocimetry (PIV) or stereo PIV, simultaneously with OH planar laser induced fluorescence. The dynamic pressure in the plenum and combustion chamber was determined by microphone probes. The flow field exhibited a conically shaped inflow of fresh gases and an inner and outer recirculation zone. The flame shape was exceptionally flat with a total height of less than 25 mm. The instantaneous flame structures were dominated by turbulent fluctuations, however, phase-correlated measurements revealed the phase-dependent changes of all measured quantities. The paper presents examples of measured results, characterizes the main features of the flame behavior, explains the feedback loop of the oscillation and discusses the flame stabilization mechanism.

1 Introduction

Swirl flames are used extensively in practical combustion systems because they enable a high energy conversion in a small volume and exhibit a good ignition and stabilization behavior over a wide operating range [1–3]. In stationary gas turbine (GT) combustors, they are mostly used as premixed or partially premixed flames and in aero engines as diffusion flames. In order to reduce NO_x emissions, the flames are operated generally very lean [4–7]. Under these conditions, the flames tend to exhibit undesired instabilities, e.g., in the form of unsteady flame stabilization or thermoacoustic oscillation [8–13]. The underlying mechanisms of the instabilities are based on the complex interaction between flow field, pressure, mixing, and chemical reactions, and are not very well understood to date. Under these conditions, combustion is governed by a complicated turbulent flow field and strong effects of turbulence-chemistry interactions. One question of interest is the flame stabilization mechanism. It is known that the mixing of recirculating exhaust gas with fresh gas plays an important role for flame stabilization, however, the details of this process are not clear. Another important question concerns the nature of the feedback mechanism of periodic combustion instabilities. Basic ideas of different feedback mechanisms have been reviewed by Lieuwen and Yang [14], but in most cases the details of the chain of events are not understood.

The investigations presented in this paper were performed at atmospheric pressure in a gas turbine model combustor with optical combustion chamber which has been used in different studies before [15–23]. At certain operating conditions the flame exhibits strong periodic thermoacoustic pulsations at a frequency of around 295 Hz. In order to investigate the mechanisms leading to flame stabilization and pulsations, various non-intrusive optical and laser measuring techniques were applied in combination with dynamic pressure measurements. For the 2D measurement of the flow field particle image velocimetry (PIV) or stereoscopic PIV were applied. The flame structures were measured by planar laser induced fluorescence of OH and by chemiluminescence imaging. Further information about the thermochemical state of the flame was gained by the use of laser Raman scattering.

2 Gas turbine model combustor and diagnostic set-up

The measurements were performed in an optically accessible model GT combustor which is a modified GT combustor originally equipped with an air blast nozzle for liquid fuels [24]. In the current measurements a non-premixed CH_4/air flame is stabilized under fuel lean conditions. The schematic of the combustor

used for the measurements is shown in Fig. 1. Co-swirling dry air fed from a common plenum at room temperature and pressure was supplied to the flame through a central nozzle (diameter 15 mm) and an annular nozzle (i.d. 17 mm, o.d. 25 mm contoured to an outer diameter of 40 mm). The plenum had an inner diameter of 79 mm and a height of 65 mm. The radial swirlers in the central and annular nozzle consisted of 8 and 12 channels respectively, resulting in a air mass flow ratio of approximately 1.5 between the annular and central nozzles. Non-swirling CH_4 was fed into the combustion chamber through 72 channels (0.5×0.5 mm), forming a ring between the air nozzles. The reference height y = 0 was defined at the exit plane of the outer air nozzle which was at a height of 4.5 mm above the exit planes of the fuel and central air nozzles. A contoured steel top plate with a central exhaust tube (diameter 40 mm, length 50 mm) formed the exhaust gas exit. The combustion chamber had a square section of 85×85 mm and a height of 114 mm and was equipped with 4 quartz windows held by 4 rods (diameter 10 mm) in the corners, thereby enabling excellent optical access to the flame zone. Air ventilators were used on the the 4 sides of the combustion chamber in order to avoid excessive over heating of the quartz windows. The high velocity in the exhaust tube avoided any backflow from outside the combustion chamber.

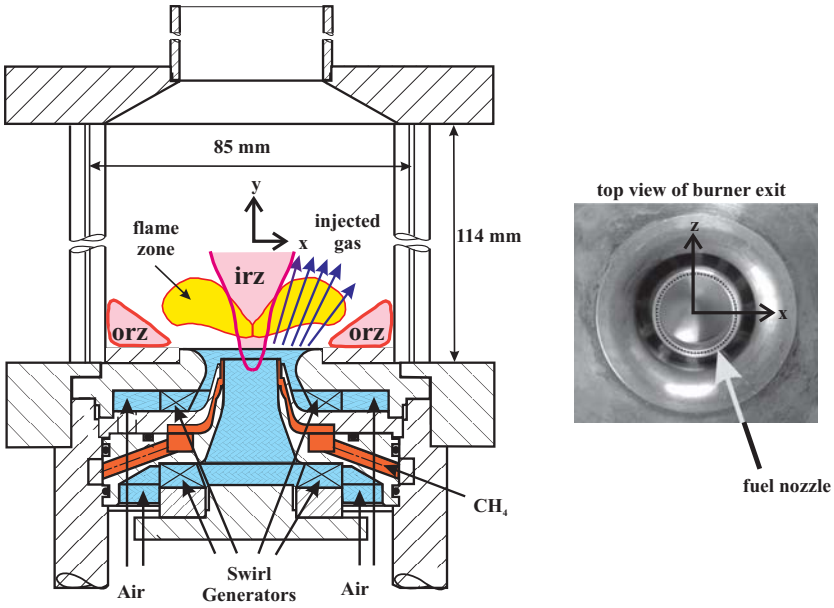

Figure 1: Schematic drawing of the GT model combustor. Also indicated are the inner and outer recirculation zones (IRZ, ORZ) together with the direction of the inflow of the gases.

The flame investigated had a thermal power (P_{th}) of 10.3 kW and an overall

equivalence ratio (ϕ) of 0.75. The corresponding CH_4 and air mass flow rates, regulated by high precision coriolis (Siemens Mass 2100) and mass flow controllers (Bronkhorst) were 12.3 g/min and 281 g/min respectively. The flame exhibited pronounced thermoacoustic oscillations at a frequency of approximately 295 Hz. Microphones (Brüel & Kjaer 4939) mounted to the plenum and to the combustion chamber, at a height of 16 mm in one of the 4 rods that held the quartz windows, were used for recording the acoustic pressure oscillations. The nozzle Reynolds number based on the cold inflow and the minimum outer nozzle diameter (25 mm) was about 15,000 and the swirl number of the burner calculated from the velocity profile just above the burner was $S \approx 0.55$ [21].

For the point wise quantitative measurement of the major species concentrations (O_2, N_2, CH_4, H_2, CO, CO_2, H_2O) and the temperature, laser Raman scattering was applied. The radiation of a flashlamp-pumped dye laser (Candela LFDL 20, wavelength λ = 489 nm, pulse energy $E_p \approx 3$ J, pulse duration $\tau_p \approx 3\ \mu$s) was focused into the combustion chamber and the Raman scattering emitted from the measuring volume (length $\approx$ 0.6 mm, diameter $\approx$ 0.6 mm) was collected by an achromatic lens (D = 80 mm, f = 160 mm) and relayed to the entrance slit of a spectrograph (SPEX 1802, f = 1 m, slit width 2 mm, dispersion $\approx$ 0.5 nm/mm). The dispersed and spatially separated signals from the different species were detected by individual photomultiplier tubes in the focal plane of the spectrograph and sampled using boxcar integrators. The species number densities were calculated from these signals using calibration measurements and the temperature was deduced from the total number density via the ideal gas law. The simultaneous detection of all major species with each laser pulse also enabled the determination of the instantaneous mixture fraction. Details of the measuring system are described elsewhere [13, 21].

The schematic of the experimental set-up used for the simulataneous PIV and OH-PLIF measurements is shown in Fig.2. Two different orientations of the light sheet was employed during the measurements: (1) in the vertical plane along the flame axis where 2D PIV and OH-PLIF measurements were performed and (2) in the horizontal plane orthogonal to the flame axis at three axial locations *y* = 5, 10 and 20 mm using 3D PIV (stereoscopic) and OH-PLIF. Due to space limitations only the results from *y* = 5 mm are shown in this paper.

The laser system used for OH-PLIF measurements consisted of a frequency doubled Nd:YAG laser (Spectra Physics, Quanta Ray PIV system) pumping a tunable dye laser (Sirah Precisionscan G-24) at 10 Hz. The frequency doubled output of the dye laser was tuned to the $Q_1(8)$ transition of OH at aprroximately 283 nm in the $\nu" = 0$, $\nu' = 1$ vibrational band of the $A^2\Sigma^+ - X^2\Pi$ system. The population of the laser-coupled ground state of the selected line varied by approximately 9 % in the temperature range of interest (1400 K$-$2200 K). The UV beam with a pulse energy of approximately 2-2.5 mJ at the laser exit was expanded into

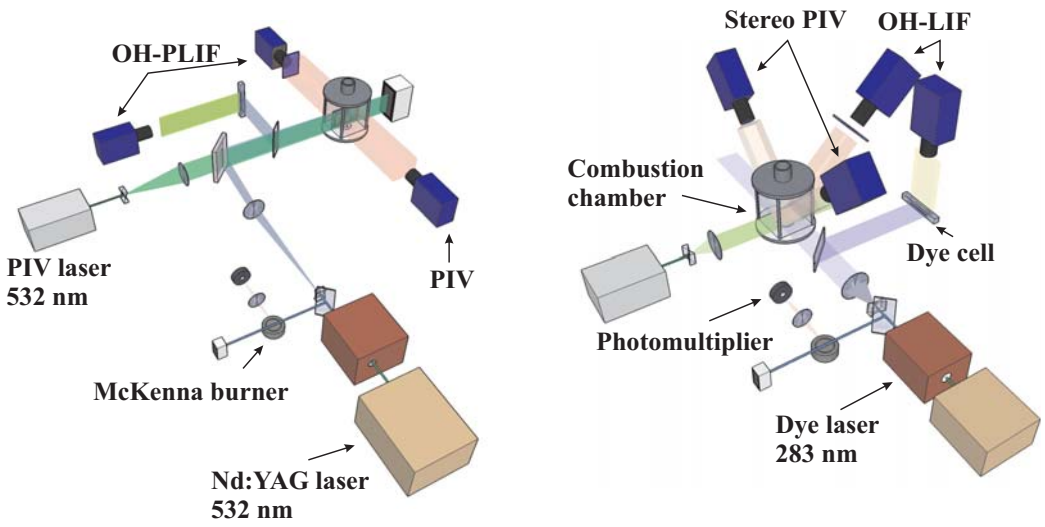

Figure 2: Schematic of the optical set-up used for simultaneous OH-PLIF and PIV measurements in the vertical orientation (left) and simultaneous OH-PLIF and stereo PIV measurements in the horizontal orientation (right).

a sheet of approximately 60 mm in height and 400 μm thickness at the burner axis using a combination of cylindrical and spherical lenses. The OH fluorescence in the $\nu' = 1$, $\nu" = 1$ and $\nu' = 0$, $\nu" = 0$ bands near 310 nm was detected by means of an interference filter in the wavelength region $295-340$ nm which also aided in blocking the unwanted scattered laser lights from OH-PLIF and PIV lasers and background radiations. Online monitoring of the excitation line was achieved by diverting a small portion of the incoming UV beam into a CH_4/air reference flame stabilised on a McKenna burner, operated under laminar conditions, and observing the intensity of the OH-LIF produced using a photomultiplier. The shot-to-shot variation in laser sheet profiles was corrected by sending a part of the incoming laser sheet on to a dye cell filled with fluorescent dye. The fluorescence emitted by this dye solution was imaged simultaneously with the OH-PLIF images and was used for correcting the laser sheet inhomogeneities in a image post processing procedure.

The OH-PLIF detection system consisted of two image intensified CCD cameras (LaVision Image Intense, 1376×1040 pixels), one for the OH-PLIF imaging and the other for the sheet profile imaging. The OH-PLIF camera was equipped with an achromatic UV lens (Halle, $f/2$, f = 64 mm)) and the sheet profile camera with a Nikon objective ($f/4$, f = 50 mm). OH* chemiluminescence was also imaged with the same detection system along with the filter combination. The exposure time for the OH-PLIF imaging was 400 ns where as for OH* chemiluminescence it was 40 μs.

In case of PIV measurements the laser system used was a frequency doubled Nd:YAG laser (New Wave Solo PIV 120) with a pulse energy of 120 mJ at 532 nm. The pulse delay between the two laser shots was 16 μs and the flow was seeded with TiO_2 particles with a nominal diameter of 1 μm. The laser beam was expanded into a sheet of 60 mm in height and 1 mm in thickess inside the combustor using a combination of cylindrical lenses. The spatial resolution of the velocities is 0.77 mm (corresponding to an interrogation region of 12×12 pixels) in both direction. The detection system consisted of two double shutter CCD cameras (LaVision Image Intense, 1376×1024 pixels) both equipped with Nikon objectives (f/5.6, f = 50 mm). The vector fields were generated using the commercially available PIV software from LaVision (Flow Master).

The time synchronisation between the different laser sources and detection systems were achieved using a programmable timing unit (PTU) from LaVision and two pulse delay generators (BNC, Model 555). The framing rate for both OH-PLIF and PIV imaging were 5 Hz. The OH-PLIF imaged was captured 10 μs after the first PIV laser pulse. This time delay also helped in mitigating the laser light scattering effects from PIV camera in addition to providing simultaneous OH-PLIF images with the velocity fields. The microphone signals from the plenum and the combustion chamber were fed into a multichannel A/D converter along with the Q-switch trigger from the lasers during the measurements for identifying the phase angle (φ) of each acquired OH-PLIF and PIV images. Here phase angle definition is such that the pressure minimum at the plenum is taken as φ = 0 degrees and the negative-to-positive transition is taken as φ = 90 degrees and so on.

3 Results and Discussions

3.1 Ensemble averaged flame and flowfield characteristics

The ensemble averaged velocity vectors overlapped over the corresponding stream lines of the flowfield at the axial plane (z = 0 mm) and at a horizontal plane (y = 5 mm) are shown in Fig.3(a). The axial plot shows a flowfield typical of enclosed swirl burners, namely an inner recirculation zone (IRZ), an outer recirculation zone (ORZ) and a conically shaped inflow of fresh gases. There are two shear layers formed, one between the fresh gases and the IRZ and the second one between the ORZ and the fresh gases. The instantaneous plots however highlighted a different picture. It was seen that small scale vortical structures are formed at the inner and outer shear layers and these vortical structures promoted intense mixing between the fresh gases and the burned gases thereby playing a vital role in the flame stabilisation and ignition of fresh mixtures [23]. The axial

velocity vectors (Vy) overlapped over the streamlines in the horizontal plane show an axisymmetric flow field at y = 5 mm. There is a strong inflow of fresh gases visible in the radial region from $x \approx$ 6-20 mm and a recirculating downward flow at the IRZ up to a radius of $x \approx$ 6 mm.

Fig.3(b) shows the ensemble averaged OH*(electronically excited) chemiluminescence and OH-PLIF images, averaged from 500 single shot images in the vertical orientation. The OH* emissions integrated along the line of sight provide information about the shape and spatial position of the heat realease zone as the near UV spontaneous emissions from OH* is visible only in the heat release zone. Also, the flame is seen to stabilise at a height of $y \approx$ 2 mm, pointing to a partially premixed flame with significant level of mixing on the way from the fuel nozzle (y = -4.5 mm) to the flame. The flame is rather flat with the region of maximum heat release extending from 5 -20 mm in the vertical direction. The disparity in the intensities seen between the left and right part of the OH-PLIF image was due to absorption by OH radicals which was $\approx$ 44% in our measurements. The absorption was determined by taking the average fluorescence intensities at two rectangular regions (5 mm wide and 10 mm high), 5 mm from the left and right side of the quartz windows at a height y = 30 mm. In order to reduce the influence of absorption and fluorescence trapping errors in the interpretation of the experimental results, only the left part of vertical OH-PLIF images and the bottom left quarter of the horizontal OH-PLIF images are used in the following sections. The OH radicals can be used as a marker for high temperature regions like reaction zones or regions of burned gases where the temperatures are $\geqslant$1400 K. So, the dark region seen in the vertical OH-PLIF image represents the cold fuel/air mixture. On comparison with the OH* images it can be concluded that the LIF intensities seen above y = 25 mm are not from the presence of reaction zones but are simply from the presence of hot burned gases.

Fig.4 shows the instantaneous images with the PIV plot overlapped over the OH-PLIF image in the vertical orientation along the axial plane (z = 0 mm) and in horizontal orientation at y = 5 mm. No strong intensity gradients are visible at the IRZ above y = 25 mm indicating the absence of reaction zones. From previous temperature measurements it is known that the temperature in this region is around 1950 K with negligible rms fluctuations, emphasizing to a region of burned gases. Also from the relatively low LIF intensities in comparison to the shear layer regions, the OH concentrations in the IRZ should be in chemical equilibrium. From the OH-PLIF image one can get a good impression of the turbulence level present at the burner exit. The wrinkled flame structures in the vertical OH-PLIF image are more or less continuous in the 2D plane like the flames in a flamelet regime. However, the flame structures in the horizontal plane near to the inner and outer shear layers are highly wrinkled with isolated regions of ignition and extinction, highlighting the strong interplay between turbulence and chemical reactions lead-

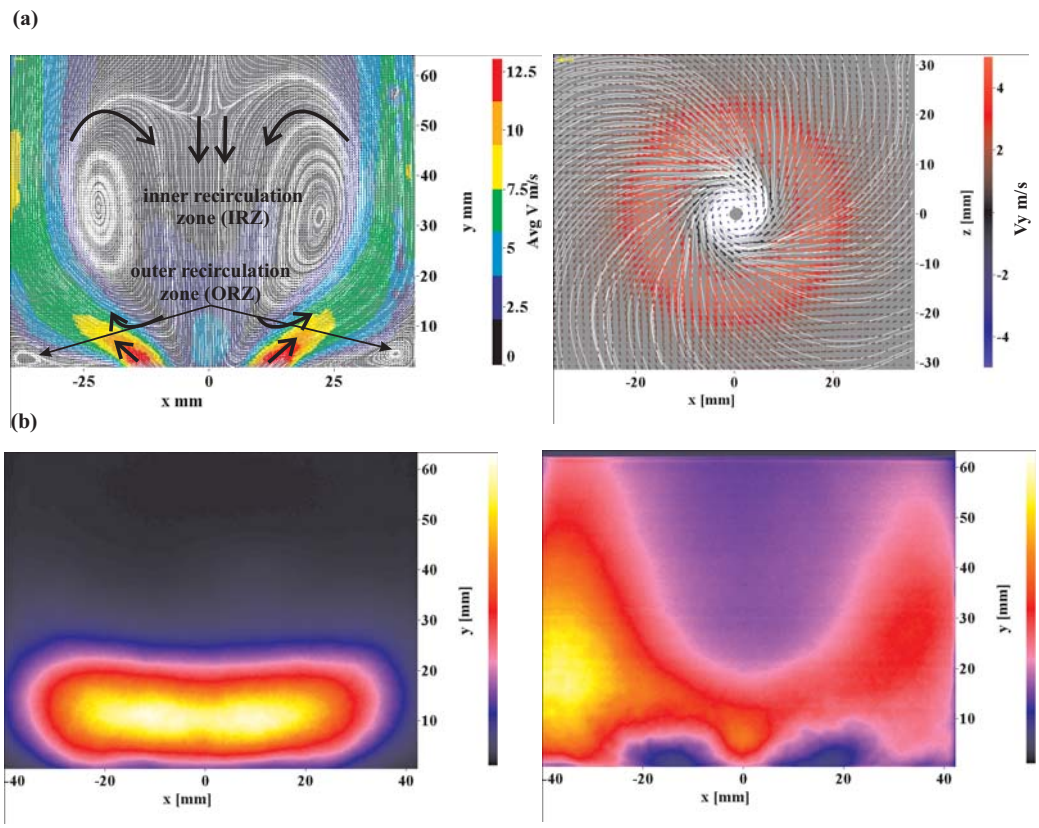

Figure 3: (a) Ensemble averaged velocities overlapped over the streamlines at the axial plane (left) and axial velocities Vy, overlapped over the streamlines at the horizontal plane, y = 5 mm (right). (b) Ensemble averaged OH* chemiluminescene image (left) and OH-PLIF image (right) in the vertical orientation.

ing to finite rate chemistry effects in this region .

3.2 Turbulence-chemistry interactions

More information on the thermochemical state of the system can be obtained from Raman scattering measurements. Fig.5 shows the temperature(T) - mixture fraction(ξ) correlation obtained from Raman scattering measurements at y = 5 mm on the same burner with similar operating conditions of fuel and air mass flow rates [18,22,25]. Here each symbol represents the result of a single shot measurement. Also shown in solid line is the result of an adiabatic flame calculation. It can be seen that the investigated flame exhibits a wide range of ξ - T combinations under such operating conditions. A large number of samples in the scatter plot lie between ξ = 0 and 0.1, highlighting the fast mixing achieved in such short

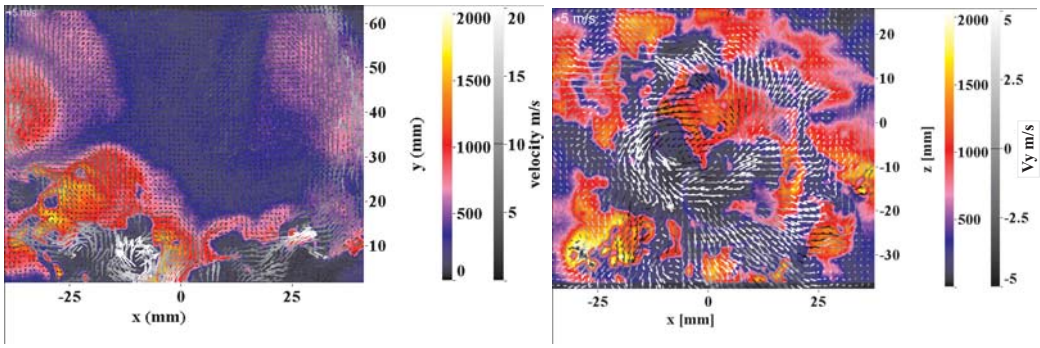

Figure 4: Instantaneous OH-PLIF and PIV images along the axial plane, z = 0 mm (left) and in the horizontal plane, y = 5 mm (right).

distances. In the IRZ (x = 0-5 mm) and ORZ (x = 27-30 mm) most of the samples lie close to the calculated curve indicating a completely reacted mixture. However in the inflow region (x = 10-15 mm) one can see samples covering a wide range of ξ - T combinations with ξ above and below the global ξ value of 0.0418 and intermediate temperatures. The wide range of T comes from mixing of the cold fuel/air mixture with the hot burned gases at the inner and outer shear layer regions. There could be two possibilities for the existence of samples with intermediate temperatures. The first one could be from mixing of fresh gas with the hot gases which rises the mixture temperature to intermediate levels and the second reason could be due to local flame extinctions which results in mixtures with temperatures far below the adiabatic temperature.

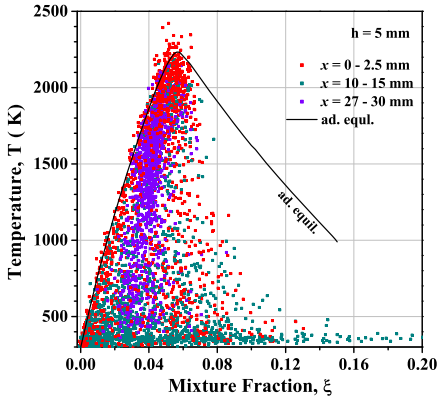

Figure 5: ξ - T correlations at y = 5 mm from Raman scattering measurements.

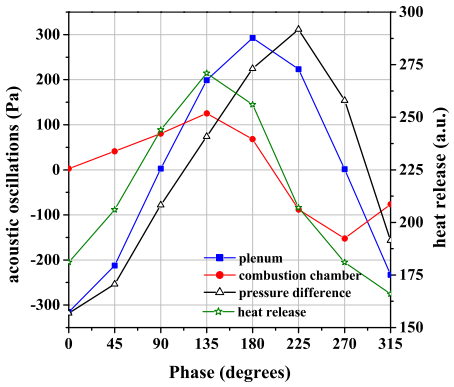

Figure 6: Relationship between the variation of plenum and combustion chamber acoustic pressure oscillations with the global heat release at different phase angles of the acoustic pressure oscillations.

3.3 Acoustic Measurements

The investigated flame exhibited strong thermoacoustic oscillations at a frequency f = 295 Hz. Fig.6 show the pressure oscillations in the plenum and combustion chamber at different φ of the acoustic oscillations. Its interesting to note that the maximum acoustic pressure in the plenum (292 Pa at φ = 180) is greater than the acoustic pressure in the combustion chamber (125 Pa at φ = 135). The pressure oscillation in the plenum is phase shifted by about 45 degrees when compared to the pressure oscillations in the combustion chamber. Also shown are the corresponding phase averaged global heat release, calculated by taking the average chemiluminescence intensity in a rectangular region covering the heat release zone in OH* chemiluminescence images at different φ . The φ corresponding to the maximum heat release matches with the maximum pressure oscillation in the combustion chamber in accordance with the Rayleigh criterion for self-sustained oscillations. The acoustic pressure difference between the plenum and the combustion chamber (δP) at different phase angles are also plotted. The δP, which reaches a maximum at around 225 degrees phase angle, is seen to have a strong influence on the acceleration of the fresh fuel/air mixture into the combustion chamber and thereby on the feed back mechanism of the combustion instability itself, as will be seen in the following sections.

3.4 Phase resolved velocity and temperature profiles

The flame shape, heat release, velocity and temperature distribution varied significantly during an oscillation cycle of the acoustic pressure. However, the instantaneous images were dominated by stochastic turbulent fluctuations and in order to reveal the phase-dependend changes, single shot results belonging to the same phase angle were averaged. The average velocity distributions at y = 5 mm for two different φ (135, 315) of the acoustic pressure oscillation and its axial component Vy overlapped over the OH-PLIF image are shown in Fig.7. It is clear from the figures that the highest OH concentrations appear at regions near to the inner and outer shear layers where the inflow velocities are moderate. These regions probably correspond to the flame zone. The inflow velocities vary significantly with φ and the IRZ is shrunk to a very intense region of burned gases with high temperatures (see discussions below) as φ changes from 135 to 315. Fig.8 shows the axial and radial velocity profiles deducted from the vertical PIV vector plots at a height of y = 2 mm for the eight phase angles. In these plots the strong periodic variations of the flowfield with φ is clearly visible. Also these plots can be used to infer qualitative information about the volumetric discharge at y = 2 mm. Going by the variations in the velocity with different φ, one can predict that there will also be a strong variation in the volumetric discharge of fresh fuel/air mixture during one complete acoustic cycle. The variations are more predominent at the inflow region, with the minimum discharge at φ = 135 and the maximum at φ = 315. Similar trends can also be seen in the IRZ where there is a stong reverse flow at φ = 135 and minimum at φ = 315. On comparison with the δP plotted on Fig.6 it can be noted that the periodic variations of the flowfield and the mass transport are affected by the pressure oscillations in the plenum and the combustion chamber. This can be witnessed in the axial and the radial velocity profiles. At the inflow region ($x \approx$ 7-18 mm), the maximum axial and radial velocities are recorded between φ = 270 and 0. That means the maximum axial velocity at φ = 315 follows approximately 90 degrees after the maximum δP at 225 degrees. This behaviour is plausible if one considers a sinusoidal form for the acoustic velocity. Then the velocity variations due to the acceleration will be phase shifted by 90 degrees which matches well with the maximum velocities. This also confirms the influence of periodic oscillations, which in turn is driven by the periodic heat release in the combustion chamber, on the mass transport. The strongest variations in the axial velocity are seen in the IRZ (0-6 m/s at x = 0 mm) and at the inflow region between x = 7-18 mm ($\approx$ 6-14 m/s) whereas the variations in the radial velocities are strong in the ORZ and the inflow region ($\approx$ 0-3 m/s and $\approx$ 6-13 m/s respectively). At φ = 270/315 the axial and radial velocities are maximum at the inflow region where as the IRZ was strongest at φ = 135/180 and the ORZ at the φ = 045. I.e., the highest inflow velocities happen 90 degrees after the

maximum δP.

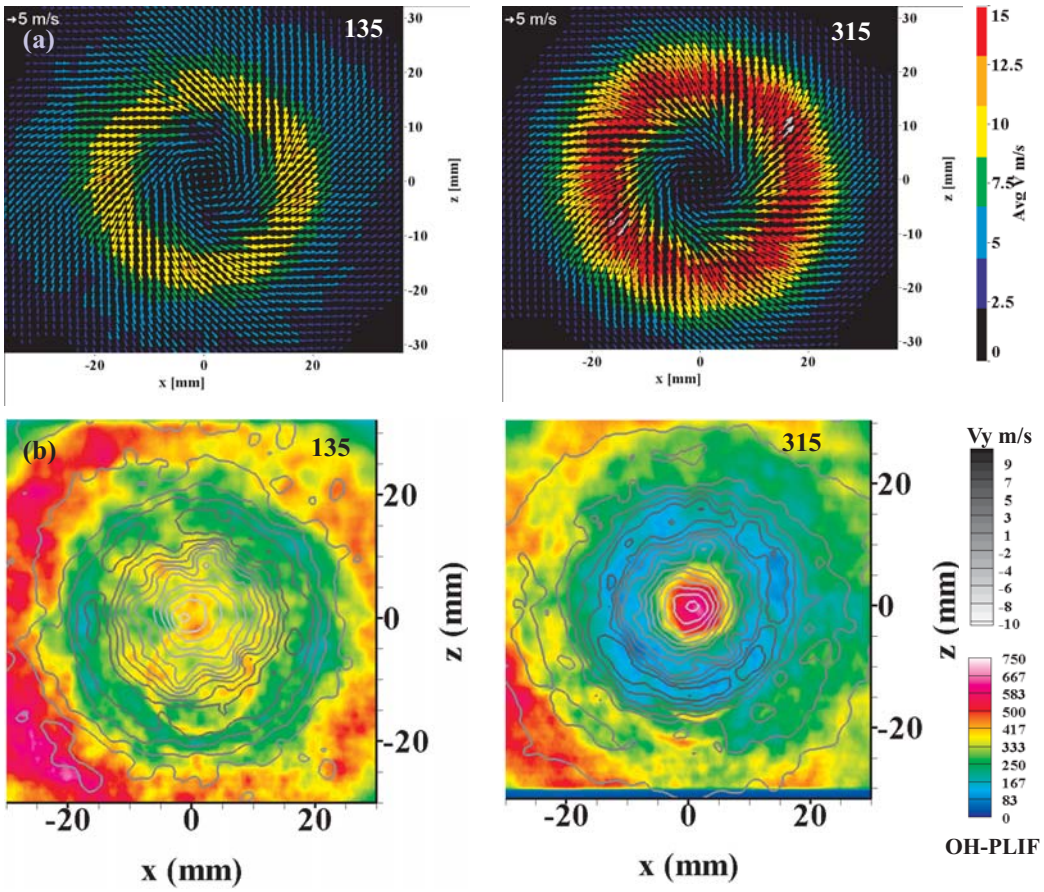

Figure 7: Average velocity distribution (a) and the axial component, Vy (b) of the average velocity overlapped over the corresponding OH-PLIF distributions for two phase angles of the acoustic pressure oscillations at *y* = 5 mm.

Radial profiles of the mean temperature (*T*) at *y* = 5 mm measured using Raman scattering experiments are shown in Fig.9 [18, 25]. Strong variations in *T* are seen in the IRZ (around 1000 K) and at the inflow region (*x* = 7-18 mm, around 300 K). The temperature in the IRZ reaches a maximum at φ = 270 and a minimum at φ = 090/135. Interestingly these φ also corresponds to the minimum and maximum recirculation velocities at the axis respectively (see Fig.8). Similarly at φ =135/180, *T* reaches a maximum at the inflow region which in turn coincides with the φ corresponding to the minimum axial velocity (φ = 135). Also, the *T* in the inflow region reaches a minimum at φ = 270/315 when the axial velocities are maximum. These varations in *T* with velocity at different φ reflect the influence of acoustic pressure oscillations, namely δP, on the themochemical state of the

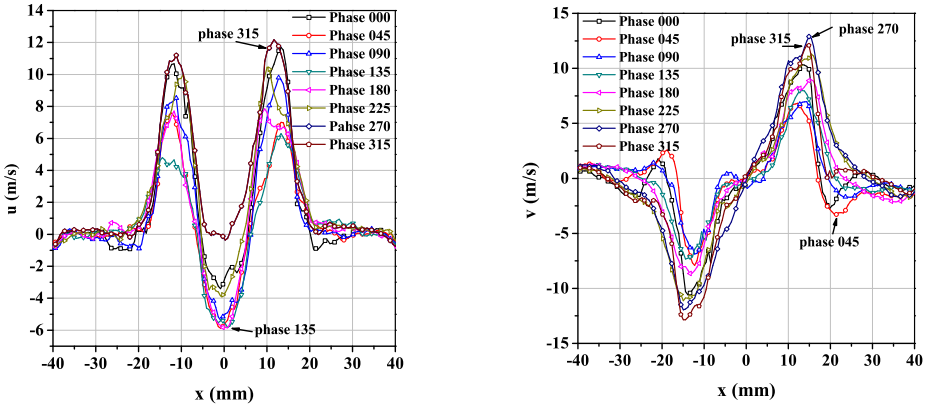

Figure 8: Axial (left) and radial (right) velocity profiles deduced from the PIV plots at y = 2 mm at different phase angles.

system at each φ by influencing the mixing and reaction rate progress.

3.5 Phase resolved heat release variations - Abel deconvoluted OH* chemiluminescence

Though OH* chemiluminescence images involve line of sight integration of intensity, in case of axisymmetric steady flames the ensemble averaged OH* images can be reprocessed to yield spatially resolved information. Fig.10 shows the Abel deconvoluted OH* chemiluminescene at four different φ (045, 135, 225, 315) representing the mean OH* distribution in the vertical plane containing the flame axis. The heat release zone extends up to a height of about 20-25 mm with the region of maxium heat release lying between y = 10-20 mm. At φ = 135 when the heat release is maximum, the flame zone extends almost to the walls of the combustion chamber whereas at φ = 315 when the heat release is minimum it reaches only to x = 30 mm. It should be noted from *section 3.4* that at φ = 135, the inflow velocity is at its minimum and at φ = 315 at maximum. Thus the heat release is half a period delayed compared to the inflow velocity (at y = 2 mm, Fig.8). The maximum inflow velocity implies a maximum mass flow into the combustion chamber because phase-dependent temperature variations are expected to be small in the inflow at y = 2 mm. Taking an average convection velocity of about 8 m/s, the distance from the inflow at y = 2 mm to the region of main heat release at about y = 15 mm takes roughly 1.6 ms which is close to half of the oscillation period of $\tau/2$ = 1.7 ms. Thus, it is plausible that the heat release variations are induced by the varying mass flow at the inflow which in turn is triggered by the pressure dif-

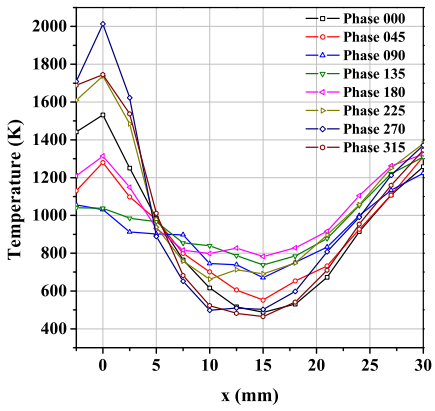

Figure 9: Radial temperature profiles at y = 5 mm for eight different φ [18].

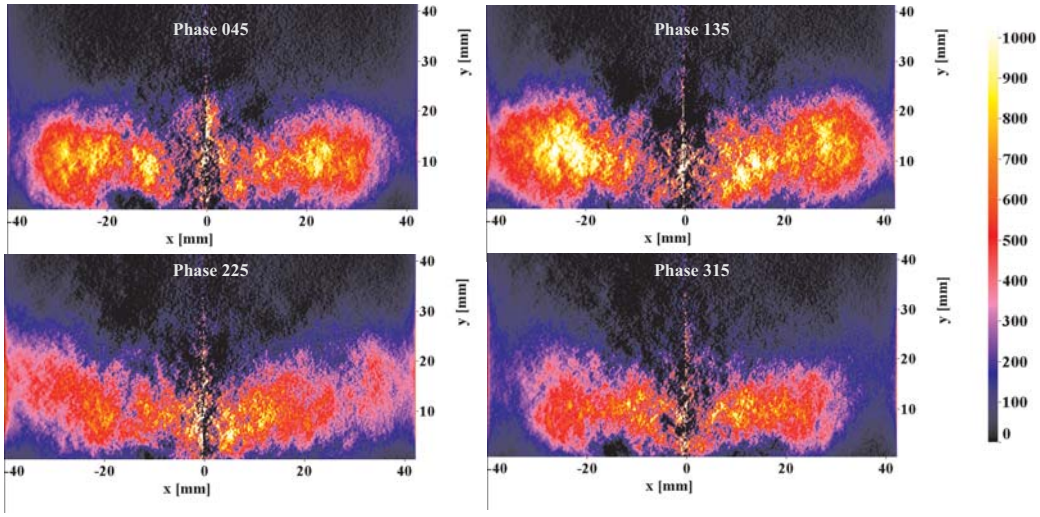

Figure 10: Abel deconvoluted OH* chemiluminescence image at four different φ of the acoustic pressure oscillation.

ference between plenum and combustion chamber. This feedback loop is known as oscillating fuel supply combined with a convective time delay and has been observed for different combustors [13, 26, 27].

With respect to the stabilization of the flame, the transport of hot combustion products within the IRZ seems to play the dominant role. From Fig.3 and Fig.4 and also from the Raman measurements it is obvious that the IRZ contains hot gases and that it reaches far down to or even into the central nozzle. The OH* distributions and single shot OH PLIF distributions [23] prove that combustion is taking place in this region, in the shear layer between inflow and IRZ. Further downstream, combustion is not only restricted to this shear layer but also seen in the region of the main inflow, as can be deducted from Fig.3 and Fig.10. At first sight it seems surprising that flame reactions can take place in the region of the high flow velocities of the inflow. From the results of this paper and further experiments [23, 28] there are indications that reacting fluid elements are convected from the shear layer into the inflow region. This process could be caused by vortex shedding or a precessing vortex core [23, 28]. Further, it is expected that a phase-dependent mixing rate of hot gas from the ORZ into the fuel/air mixtures of the inflow contributes to the reactivity of the mixtures and the stabilization of the flame [19]. Finally, phase-dependent changes of the strain rates within the inflow might also have an influence on the flame stabilization.

4 Conclusions and Outlook

A non-premixed CH_4/air flame has been operated in a gas turbine model combustor with good optical access. Various measuring techniques have been applied for the investigation including chemiluminescence imaging, (stereo) PIV, laser Raman scattering, PLIF of OH and dynamic pressure recording. At 10.3 kW thermal power and a global equivalence ratio of 0.75, the flame exhibited strong thermoacoustic oscillations at a frequency of around 295 Hz. In this flame, the ensemble averaged velocity fields and chemiluminescence images showed a flowfield typical of enclosed swirl flames with an inner and outer recirculation zone and a conical inflow region between them. The region of heat release was relatively short and extended only up to a height of 20-25 mm. Single shot PIV/PLIF measurements revealed that the instantaneous distributions of velocity and OH were dominated by turbulent structures with typical sizes of several millimeters. The thermochemical state of the flame, as deduced from Raman measurements, was characterized by a large spread in reaction progress reaching from non-reacted via partially reacted to completely reacted. The phase-correlated measurements showed that all measured quantities varied with the acoustic frequency of the flame. The heat release as deduced from the OH* distributions was in phase with

the pressure in the combustion chamber. The pressure in the plenum ran ahead of the pressure in the combustion chamber by about 45 degree and the pressure difference was seen to trigger the phase-dependent changes of the inflow velocity and thus the mass flow into the combustion chamber. The measured results led to the conclusion that the varying inflow is the main reason for the varying heat release. I.e. the feedback loop of the oscillations is an oscillating fuel supply combined with a convective time delay.

With respect to the shape of the flame and the stabilization mechanism there remain open questions. It became obvious that the inner recirculation zone played an important role by convecting hot combustion products to the flame root, as in many other swirl flames. However, one particular feature of this flame is the rather flat shape and the occurrence of reaction within the area of the high flow velocities of the inflow. There were indications that reacting fluids elements are ripped from the inner shear layer and transported into the inflow region and thereby igniting and burning the fresh gases. The driving force for that process might be a precessing vortex core. However, further effects like mixing of hot gas from the outer recirculation zone into the injected fresh gas or phase-dependent changes of the turbulence scales might also contribute to the flame shape. Here, combined PIV and OH PLIF measurements with pulse repetition rates of several kilohertz are planned to yield a deeper insight into the complex processes.

5 Acknowledgement

The work has been financially supported within the DLR research project "Mehrskalen-Verbrennungssimulation".

References

[1] A. Gupta, D. Lilley, N. Syred, Swirl Flows, Abacus Press, Kent, 1984.

[2] N. Syred, J. Beér, Combustion in swirling flows: A review, Combustion and Flame 23 (1974) 143–210.

[3] R. Weber, J. Dugué, Combustion accelerated swirling flows in high confinements, Progress in Energy and Combustion Science 18 (1992) 349–367.

[4] S. Correa, Power generation and aero propulsion gas turbines from combustion science to combustion technology, Proceedings of the Combustion Institute 27 (1998) 1793–1807.

[5] A. Lefebvre, Gas Turbine Combustion, Taylor & Francis, Philadelphia, 1999.

[6] H. Bauer, New low emission strategies and combustor designs for civil aero engine applications, Progress in Computational Fluid Dynamics 4 (2004) 130–142.

[7] K. Syed, E. Buchanan, The nature of NOx formation within an industrial gas turbine dry low emission combustor, Proceedings of ASME Turbo Expo, Nevada, USA GT-2005-68070.

[8] J. Keller, Thermoacoustic oscillations in combustion chambers of gas turbines, AIAA Journal 33 (1995) 2280–2287.

[9] C. Paschereit, E. Gutmark, W. Weisenstein, Structure and control of thermoacoustic instabilities in a gas turbine combustor, Combustion Science and Technology 138 (1998) 213–232.

[10] S. Candel, Combustion dynamics and control: Progress and challenges, Proceedings of the Combustion Institute 29 (2002) 1–28.

[11] J. Lee, D. Santavicca, Experimental diagnostics for the study of combustion instabilities in lean premixed combustors, Journal of Propulsion and Power 19 (2003) 735–750.

[12] N. Syred, A review of oscillation mechanisms and the role of precessing vortex core (PVC) in swirl combustion systems, Progress in Energy and Combustion Science 32 (2006) 93–161.

[13] W. Meier, P. Weigand, X. Duan, R. Giezendanner-Thoben, Detailed characterization of the dynamics of thermoacoustic pulsations in a lean premixed swirl flame, Combustion and Flame 150 (2007) 2–26.

[14] T. Lieuwen, V. Y. (Eds.), Combustion Instabilities in Gas Turbine Engines : Operational Experience, Fundamental Mechanisms, and Modeling, American Institute of Aeronautics and Astronautics, Inc., Reston, Virginia, 2006.

[15] R. Giezendanner, O. Keck, P. Weigand, W. Meier, U. Meier, W. Stricker, M. Aigner, Periodic combustion instabilities in a swirl burner studied by phase-locked planar laser-induced fluorescence, Combustion Science and Technology 175 (2003) 721–741.

[16] X. Duan, P. Weigand, U. Meier, O. Keck, B. Lehmann, W. Stricker, M. Aigner, Experimental investigations and laser based validation measurements in a gas turbine model combustor, Progress in Computational Fluid Dynamics 4 (2004) 175–182.

[17] W. Meier, X. Duan, P. Weigand, Reaction zone structures and mixing characteristics of partially premixed swirling CH_4/air flames in a gas turbine model combustor, Proceedings of the Combustion Institute 30 (2005) 835–842.

[18] X.R.Duan, W. Meier, P. Weigand, B. Lehmann, Phase-resolved laser Raman scattering and laser Doppler velocimetry applied to periodic instabilities in a gas turbine model combustor, Applied Physics B 80 (2005) 389–396.

[19] P. Weigand, W. Meier, X. Duan, R. Giezendanner, U. Meier, Laser diagnostic study of the mechanism of a periodic combustion instability in a gas turbine model combustor, Flow, Turbulence and Combustion 75 (2005) 275–292.

[20] R. Giezendanner, U. Meier, W. Meier, J. Heinze, M. Aigner, Phase-locked two-line OH-PLIF thermometry in a pulsating gas turbine model combustor at atmospheric pressure, Applied Optics 44 (2005) 6565–6577.

[21] P. Weigand, W. Meier, X. Duan, W. Stricker, M. Aigner, Investigations of swirl flames in a gas turbine model combustor I. flow field, structures, temperature, and species distributions, Combustion and Flame 144 (2006) 205–224.

[22] W. Meier, X. Duan, P. Weigand, Investigations of swirl flames in a gas turbine model combustor II. turbulence-chemistry interactions, Combustion and Flame 144 (2006) 225–236.

[23] R. Sadanandan, M. Stöhr, W. Meier, Simultaneous OH-PLIF and PIV measurements in a gas turbine model combustor, Applied Physics B 90 (2008) 609–618.

[24] M. Cao, H. Eickhoff, F. Joos, B. Simon, Influence of operating conditions on the atomisation and distribution of fuel by air blast atomizers, ASME Propulsion and Energetics Panel 70^{th} Symposium, Crete 422 (1987) S.8.1–8.8.

[25] P. Weigand, Untersuchung periodischer Instabilitäten von eingeschlossenen turbulenten Drallflammen mit Lasermessverfahren, DLR Forschungsbericht 2007-19, Stuttgart, 2007.

[26] T. Sattelmayer, Influence of the combustor aerodynamics on combustion instabilities from equivalence ratio fluctuations, Jorunal of Engineering of Gas Turbines and Power 125 (2003) 11–19.

[27] M. Zhu, A. Dowling, K. Bray, Forced oscillations in combustors with spray atomizers, Jorunal of Engineering of Gas Turbines and Power 124 (2002) 20–30.

[28] M. Stöhr, R. Sadanandan, W. Meier, Experimental study of unsteady flame structures of an oscillating swirl flame in a gas turbine model combustor, Proceedings of the Combustion Institute *accepted*.